

Award Accounts

The Chemical Society of Japan Award for Creative Work for 2012

Nonadiabatic Electronic Dynamics in Isolated Molecules and in Solution Studied by Ultrafast Time–Energy Mapping of Photoelectron Distributions

Toshinori Suzuki[1,2,3]

[1]Department of Chemistry, Graduate School of Science, Kyoto University, Kyoto 606-8502

[2]CREST, Japan Science and Technology Agency, Tokyo 102-0076

[3]RIKEN Center for Advanced Photonics, RIKEN, Wako, Saitama 351-0198

Received October 4, 2013; E-mail: suzuki@kuchem.kyoto-u.ac.jp

Nonadiabatic electronic dynamics contribute to the diversity of chemical reactions. We investigate nonadiabatic dynamics in isolated molecules and aqueous solutions by time-resolved photoelectron spectroscopy. For isolated molecules in the gas phase, we combine two-dimensional imaging detection of electrons and a sub-20 fs deep UV and vacuum UV light source to measure time-evolution of the photoelectron kinetic energy and angular distributions. Time–energy mapping of photoelectron angular anisotropy reveals the $S_2 \rightarrow S_1$ internal conversion dynamics through conical intersection in pyrazine, benzene, and toluene. The time–energy mapping is also employed to extract the photoelectron angular distribution in the molecular frame for nitric oxide. For electronic dynamics in aqueous solution, we employ time-resolved photoelectron spectroscopy using a liquid beam and an electrostatic or a time-of-flight electron energy analyzer. Successful observation of ultrafast electron-transfer reactions in aqueous solutions and measurement of electron binding energies of solvated species suggest promising future developments of this very young field.

1. Introduction

The structures and dynamics of molecules are determined by quantum mechanics, while the quantum mechanical equation of motions of the nuclei and electrons is not exactly solvable. Born and Oppenheimer have approximated the rigorous equation by separating it into a set of equations of the nuclei and of the electrons, which facilitated a quantum mechanical description of chemistry.[1] Based on the approximation, a chemical reaction is understood as quantum-mechanical nuclear motion on an adiabatic potential energy surface created by electronic motions. The approximation, however, breaks down at critical nuclear configurations where multiple electronic states have similar energies. Consequently, nonadiabatic transitions (or hoppings) occur between different potential energy surfaces in the vicinities of these critical configurations. The nonadiabatic transitions change reaction pathways and product yields, contributing to the diversity of chemical reactions.

Nonadiabatic transitions are ubiquitous in the excited state dynamics of polyatomic molecules, because polyatomic molecules have a large number of excited electronic states within a narrow energy range, which cause (avoided) crossings of potential energy surfaces. The conical intersection is one of the most important topographic features of the surface crossings for nonadiabatic transitions.[2–5] Figure 1 shows photochemical reaction pathways mediated by conical intersections of the potential energy surfaces in benzene.[6] The characteristic funnel shape of the conical intersection facilitates efficient draining of a nuclear wave packet from an upper to a lower potential energy surface. Although remarkable progress has been made in our understanding of chemical reactions in the past 30 years, nonadiabatic dynamics of polyatomic molecules remain highly challenging subjects of research. Direct experimental observation of ultrafast electronic dynamics and interplay with theoretical calculations are indispensable in this research field.

Photoelectron (photoemission) spectroscopy is an experimental method based on the photoelectric effect, and it was initiated in the late 1950s to early 1960s.[7–9] One of the pioneers of photoelectron spectroscopy, Kai Siegbahn, received the Nobel Prize of Physics in 1981.[10] Photoelectron spectroscopy induces emission of an electron from a material using a photon beam (such as UV or X-ray radiation) and measures the kinetic energies of photoelectrons. Time-resolved photoelectron spectroscopy (TRPES) is an advanced form of photoelectron spectroscopy using a pair of laser pulses.[11–15] The pump pulse creates a wave packet in an electronically excited state, and the probe pulse interrogates its time-evolution by photoemission. TRPES requires the laser pulse durations to be shorter than the

Published on the web March 15, 2014; doi:10.1246/bcsj.20130272

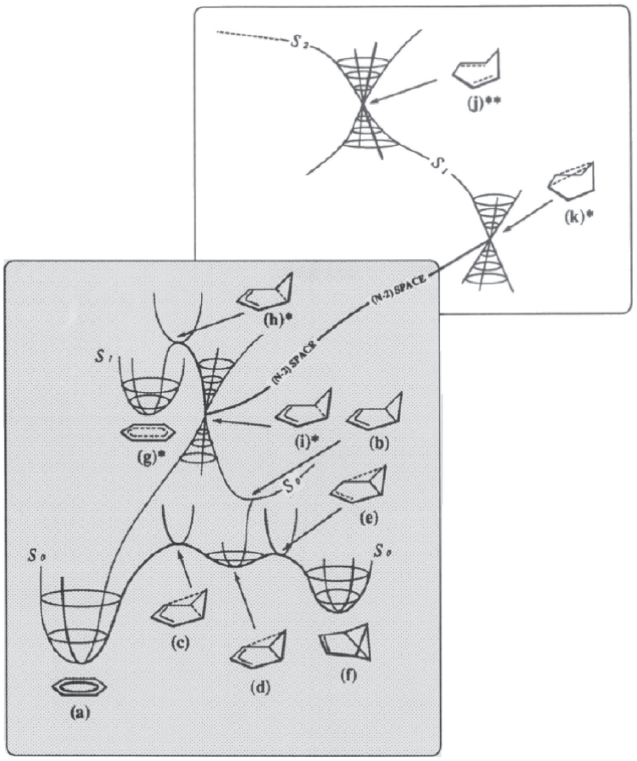

Figure 1. Photochemical reactions of benzene from S_2 and S_1 states mediated by conical intersections. Reproduced with permission from Ref. 6.

time scales of the dynamics of interest and the pulse energies sufficiently high to induce ionization within the pulse durations. A highly sensitive electron detection method is also important for TRPES, because the number of photoelectrons generated per optical pulse-pair must be minimized to avoid electrostatic repulsion between the photoelectrons, which would otherwise alter the electron kinetic energies.

Ionization has several important advantages as a probing method of chemical reactions. First of all, the final state is energetically continuous, so that ionization can be induced from any part of the excited state potential energy surfaces as long as the photon energy is sufficient. Second, the ionization continuum is degenerate for different symmetries and spin states of photoelectrons, so that ionization is almost always an allowed transition; the singlet and triplet excited states are equally observed. Third, high sensitivity can be obtained by collecting photoelectrons using electromagnetic fields.

We employ TRPES of gas-phase reactions to elucidate fundamental aspects of electronic dynamics in elementary chemical reactions. The dynamics, however, are significantly altered in solution, especially in polar protic solvents such as water. While solvent effects have been employed for centuries to control solution chemistry, the coupled electronic and solvation dynamics in solution are not well understood. Therefore, it is highly interesting to develop TRPES of liquids to tackle this classic problem in chemistry. Since the 1970s, there has been a long history of endeavors to bring volatile liquids into high vacuum photoelectron spectrometers.[16] For an example, intriguing devices such as a rotating wire and a rotating trundle wetted with a sample solution were developed for this purpose.[16] A high-speed liquid microjet reduced the difficulty, since a small diameter (ca. 10–20 μm) minimizes the surface area from which solvents evaporate, and a high speed minimizes the temperature drop in the transport from the nozzle to the ionization point.[17] The temperature of water jet at 1 mm downstream of the nozzle is estimated to be 5–10 °C.[18] We devoted our own efforts to develop TRPES of liquids for a decade and succeeded for the first time in 2010.[19,20]

This article is organized as follows. In Section **2**, I describe TRPES of gas-phase reactions using two-dimensional photoelectron imaging and a novel ultrafast laser in the deep UV (DUV) and vacuum UV (VUV) regions. The key technique is time–energy mapping of photoelectron angular anisotropy, which provides information on electron configuration of the nonstationary state. We examine ultrafast internal conversion in isolated molecules of pyrazine, benzene, and toluene and discuss their differences. In Section **3**, I describe extraction of the molecular-frame photoelectron angular distribution, seen by an observer on a molecule, using the time–energy mapping of photoelectron angular anisotropy. Section **4** is devoted to the new research area of TRPES of liquids. An electron-transfer reaction in water and generation of a hydrated electron are discussed. Section **5** presents the summary and perspectives for future studies.

2. Ultrafast Internal Conversion in Isolated Aromatic Molecules Studied by Time-Resolved Photoelectron Imaging Using a Sub-20 fs DUV/VUV Light Source

2.1 Experimental Technique. When photoelectron spectroscopy was initiated in the 1950s using continuous light sources, experiments were performed using electrostatic electron energy analyzers.[7–9] Although these analyzers are still principal instruments in high-resolution X-ray photoelectron spectroscopy today, relatively long integration times of the signals are required owing to small solid angles and narrow energy windows. With the development of intense pulsed (nanosecond and picosecond) lasers, photoelectron spectroscopy using multiphoton ionization started in the 1980s, which employed time-of-flight (TOF) photoelectron spectrometers. The TOF spectrometer measures flight times of photoelectrons from a sample to a detector, and it enables measurement of the entire photoelectron energy spectrum on a shot-to-shot basis. Furthermore, a magnetic bottle was introduced to achieve an electron collection efficiency of 50% with the TOF analyzer, which enabled the application of photoelectron spectroscopy to low-density species such as molecular and metal clusters in supersonic beams.[21] However, a photoelectron angular distribution can hardly be measured with a magnetic bottle, as it utilizes electron cyclotron motions in a magnetic field.

Chandler and Houston invented an ion imaging technique in 1988, in which ions emitted from a small target volume in a Wiley-McLaren TOF mass spectrometer are accelerated and projected onto a two-dimensional (2D) position-sensitive detector.[22] Eppink and Parker have modified the ion optic electrodes and enabled 2D space focusing of ions to improve the imaging resolution.[23] Their method is now called velocity map imaging, because the arrival position of the ion on the detector plane is proportional to the velocity perpendicular

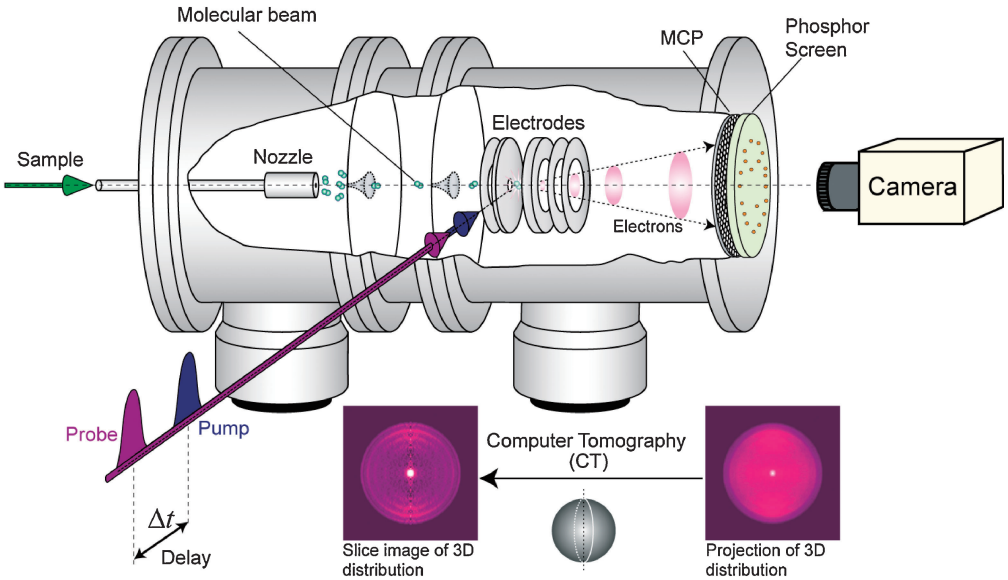

Figure 2. Time-resolved photoelectron imaging apparatus.

to the flight axis and independent of the ionization point. The performance of acceleration electrodes (aberration etc.) can be further improved by increasing number of electrodes beyond the Eppink–Parker minimal design which uses three electrodes.[24,25]

We combined the femtosecond pump–probe method and 2D imaging technique to initiate time-resolved photoelectron imaging (TRPEI) in 1999.[26,27] Figure 2 shows a schematic diagram of TRPEI.[28–30] An ultracold gas of target molecules is created by adiabatic gas expansion into vacuum, and the gas jet is skimmed to create a supersonic molecular beam 2 mm in diameter. The beam is introduced into a photoelectron spectrometer and crossed with the pump and probe laser beams. The pump pulse excites molecules to excited electronic states, and the probe pulse induces photoemission to create an expanding sphere of a photoelectron distribution. The photoelectrons are accelerated in a static electric field and projected onto a position-sensitive detector. The detector consists of microchannel plates, a phosphor screen, and a CCD (or CMOS) camera, and it records the arrival positions of the photoelectrons on the detector plane. Since both the pump and probe laser polarizations are parallel to each other and to the detector face, the original 3D distribution has axial symmetry around the polarization direction. With this symmetry, the 3D distribution can be reconstructed from the projection image. The advantage of TRPEI over other methodologies is the ability to measure time-evolution of the photoelectron angular distribution (PAD) with high efficiency and accuracy. We developed a 2D electron-counting apparatus using a CMOS camera and real-time centroiding calculations on a field programmable gate array circuit, which captured electron images at 1 kHz with a uniform sensitivity over the detector area.[31] The imaging detector is able to record simultaneous arrivals of many electrons, which is an advantage over other 2D position-sensitive detectors such as delay-line detectors.

The photoelectron ejection angle is an important observable in photoelectron spectroscopy. Since the initial ensemble of molecules has an isotropic molecular axis distribution in the absence of an external field, it is an isotropic target for photoionization, similar to the 1s orbital of a hydrogen atom. Therefore, the anisotropy of the total physical system (molecule + radiation) prior to photoionization is caused by polarized photons. This anisotropy is transferred to the PAD after photoionization. For linear polarization of the pump and probe pulses parallel to each other, the photoelectron kinetic energy and angular distribution in $[1 + 1']$ photoionization is expressed as follows (the prime means different color):

$$I(t, E, \theta) = \frac{\sigma(t, E)}{4\pi}\{1 + \beta_2(t, E)P_2(\cos\theta) + \beta_4(t, E)P_4(\cos\theta)\} \quad (1)$$

where t, θ, and E are the pump–probe time delay, the electron ejection angle from the laser polarization direction, and the photoelectron kinetic energy. $P_n(x)$ are the n-th order Legendre polynomials. $\sigma(t,E)$ represents a photoelectron kinetic energy distribution or photoelectron spectrum. $\beta_2(t,E)$ and $\beta_4(t,E)$ are called anisotropy parameters, and the three scalar quantities $\sigma(t,E)$, $\beta_2(t,E)$, and $\beta_4(t,E)$ in eq 1 are the observables in $[1 + 1']$ TRPEI of gaseous samples.

Now we consider laser requirements in TRPEI experiments by considering the most fundamental aromatic molecule of benzene. Its ionization energy is 9.24 eV, so that one-photon ionization of benzene requires an ionization laser wavelength shorter than 134 nm, and the pump–probe TRPES requires at least one of the pump or probe wavelengths to be shorter than 268 nm. One of the characteristic molecular vibrations of benzene is a totally symmetric ring-breathing mode with a vibrational period of ca. 50 fs. In order to create a spatially localized wave packet and observe its time evolution, the pump and probe pulses should be sub-30 fs. While tunable DUV pulses down to ca. 200 nm can be generated using optical parametric amplifiers and nonlinear optical crystals, a VUV pulse can hardly be generated by these methods. The pulse durations are also generally longer than 30 fs. Thus, we devel-

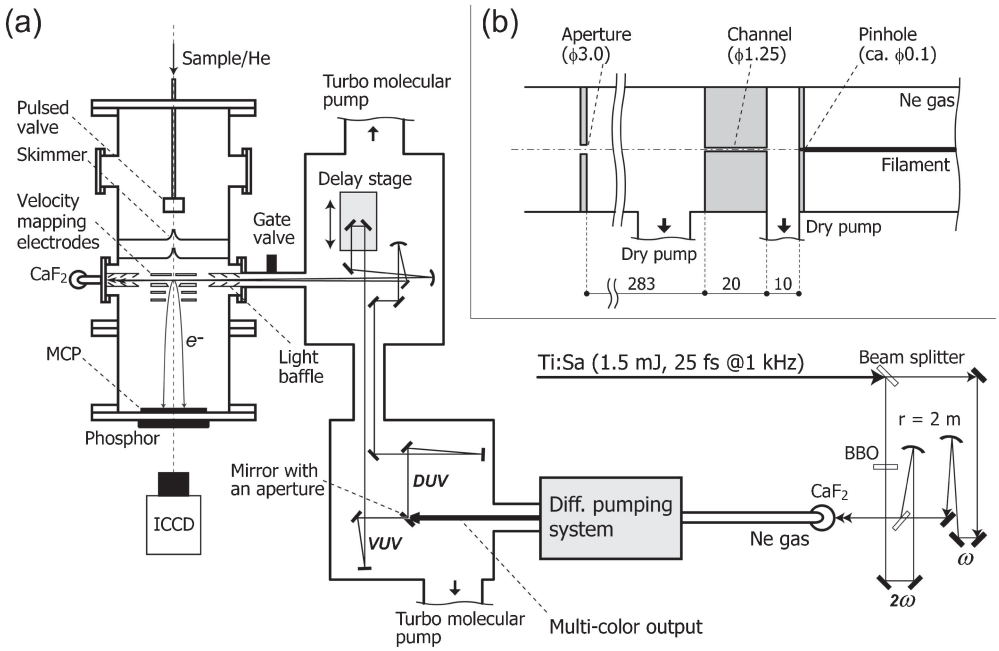

Figure 3. (a) Schematic diagram of the experimental setup. (b) Schematic drawing of the differential pumping system. All dimensions are given in millimeters.

oped a filamentation four-wave mixing method[32–34] in rare gas to generate sub-20 fs DUV and VUV pulses (Figure 3). Filamentation is a unique propagation scheme of an intense laser pulse through a medium. An intense laser pulse alters the refractive index of the medium (optical Kerr effect), which induces self-focusing of the pulse; however, as the focused laser pulse induces (tunnel-)ionization of the medium, the ionized species create an opposite spatial gradient of the refractive index. Consequently, the laser pulse propagates through the medium as a tightly focused beam for a distance longer than the Rayleigh length,[35] which facilitates efficient wavelength conversion in low density gases.

In our experiment, the fundamental (ω: 775 nm, 25 fs) and the second harmonic (2ω: 390 nm, 30 fs) of a Ti:sapphire laser are gently focused into a neon gas inducing the filamentation four-wave mixing process of $2\omega + 2\omega - \omega \rightarrow 3\omega$ (264 nm). Then, the cascaded four-wave mixing processes generate 4ω (198 nm), 5ω (159 nm), and 6ω (134 nm) pulses simultaneously. The DUV and VUV pulses are transmitted through a pinhole placed at the end of the neon gas cell. The central and peripheral parts of the output beam are separated spatially, and different harmonics are isolated using dichroic mirrors. The two different harmonics are independently focused onto a molecular beam with two concave mirrors. The cross-correlation between 4ω and 5ω is 18 ± 2 fs.

2.2 $S_2 \rightarrow S_1$ Internal Conversion via a Conical Intersection in Pyrazine. Pyrazine was one of the first molecules studied with TRPES in 1999.[27] The $S_2(^1B_{2u}, \pi\pi^*) \rightarrow S_1(^1B_{3u}, n\pi^*)$ internal conversion of pyrazine ($C_4H_4N_2$, D_{2h}) is the best-known example of ultrafast electronic deactivation mediated by a conical intersection. The low-lying conical intersection between the S_2 and S_1 potential energy surfaces of pyrazine was identified in 1988.[36] Thereafter, a number of theoretical studies have been performed on this system.[37–50] Although

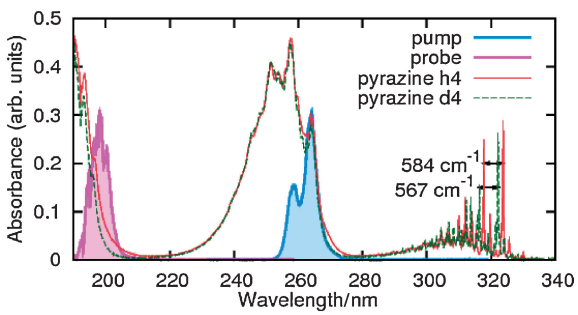

Figure 4. UV photoabsorption spectra of S_1, S_2, and S_3 of pyrazine-h_4 (thin solid line) and pyrazine-d_4 (thin dashed line) at room temperature. The spectra of our pump (264 nm, 4.70 eV) and probe (198 nm, 6.26 eV) pulses are also shown in solid lines.

pyrazine has 24 normal modes, only a single mode Q_{10a} (b_{1g}) mediates the S_2–S_1 coupling, and a few totally symmetric (a_g) modes play principal roles in the vibrational dynamics. Seel and Domcke proposed TRPES of pyrazine theoretically in 1991 using model calculations taking into account three vibrational coordinates of Q_1, Q_{6a}, and Q_{10a}.[51] Theoretical studies have predicted that the internal conversion occurs within 30 fs, while the time resolution of our experiment in 1999 was 450 fs.[26,27] Thus, we constructed a sub-20 fs DUV laser using filamentation four-wave mixing and revisited the S_2–S_1 dynamics of pyrazine in 2010.[52]

Figure 4 shows the UV photoabsorption spectra of pyrazine (pyrazine-h_4) and fully deuterated pyrazine (pyrazine-d_4) vapor measured at room temperature. Overlaid are the spectra of our 3ω (264 nm: blue) and 4ω (198 nm: red) pulses. The 3ω pulse excites pyrazine to S_2 near the origin and the 4ω pulse ionizes from S_2 and S_1. However, the 4ω pulse overlaps (unfavorably)

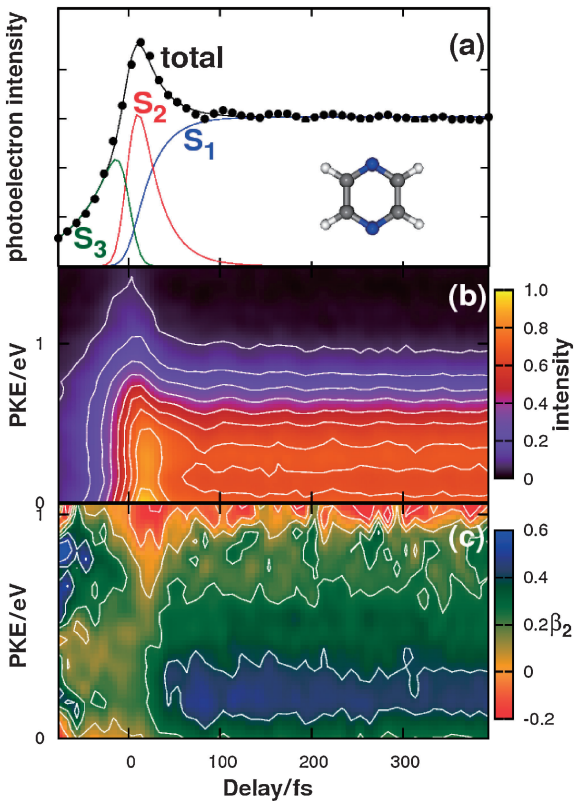

Figure 5. (a) Temporal profile of total photoelectron signal in 3ω–4ω TRPEI of pyrazine-h_4. The observed profile is well explained by three components: single-exponential decay of S_2 (red); corresponding increase in S_1 (blue) for positive time delays; and single-exponential decay of S_3 (green) for negative time delays. The fitting result is shown as a solid line. (b) Time-evolution of photoelectron kinetic energy (PKE) distribution, $\sigma(t,E)$. (c) Time evolution of the photoelectron angular anisotropy parameter $\beta_2(t,E)$.

with the S_3–S_0 band, and the 4ω–3ω pulse sequence in the negative time delays also creates a photoelectron signal.

Figure 5a shows the total photoelectron signal intensity as a function of the pump–probe time delay. For positive time delays with the 3ω–4ω pulse sequence, the total signal intensity rapidly decays within the first 30 fs and exhibits a plateau at later times: our previous experiment in 1999 has shown that this long-lived component has a finite lifetime of 22 ps for pyrazine-h_4.[27,53] For negative time delays with the 4ω–3ω pulse sequence, the signal decays within 50 fs. These time profiles, therefore, consist of three components corresponding to the decay of optically excited S_2 (red), the corresponding growth of S_1 (blue) populated by internal conversion from S_2, and the decay of S_3 (green), respectively. Using least-squares fitting, the $S_2 \rightarrow S_1$ internal conversion time constants are estimated as 23 ± 4 fs for pyrazine-h_4 and 20 ± 2 fs for pyrazine-d_4. The plateau region exhibits oscillatory features due to vibrational quantum beats of Q_{6a} in S_1 (583 cm^{-1}).

Figure 5b shows the photoelectron kinetic energy distributions measured at each time delay. Although the $S_2 \rightarrow S_1$ internal conversion occurs within 30 fs, no marked change is observed here. This is because photoionization predominantly

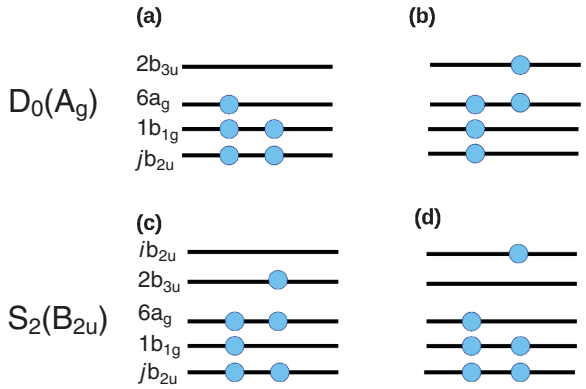

Figure 6. Main configurations of (a) D_0 and (c) S_2 and relevant configurations for one-photon ionization of $D_0 \leftarrow S_2$, (b) and (d).

occurs as $D_0(n^{-1}) \leftarrow S_1(n,\pi^*)$ and $D_1(\pi^{-1}) \leftarrow S_2(\pi,\pi^*)$ and the energy differences are almost identical between D_1 and D_0 (0.88 eV)[54] and between S_2 and S_1 (0.86 eV).[55]

Figure 5c shows the time and energy dependence of the anisotropy parameter $\beta_2(t,E)$; the positive (blue-green) and negative (red) values correspond to preferential ejection of an electron parallel and perpendicular to the probe laser polarization (eq 1). The energy-dependence of β_2, a stripe of colors at each time delay in Figure 5c, is the fingerprint of the electronic character. In the region of $t < 30$ fs, high-energy electrons are ejected perpendicularly to the probe laser polarization (red), while low-energy electrons are distributed almost isotropically (green). After 30 fs, the high-energy electron distribution becomes isotropic, while low-energy electrons are preferentially ejected parallel to the probe laser polarization (blue). The sudden change of the color at ca. 30 fs indicates the occurrence of $S_2 \rightarrow S_1$ internal conversion, in agreement with the analysis of the total electron signal.

In Figure 5c, the photoelectron kinetic energy component of 0.8–1.0 eV appearing within 30 fs is attributed to photoionization from $S_2(\pi,\pi^*)$ to $D_0(n^{-1})$. As shown in Figure 6, the main electron configurations of $S_2(\pi,\pi^*)$ to $D_0(n^{-1})$ cannot be connected by a one-electron process. The occurrence of the $D_0(n^{-1}) \leftarrow S_2(\pi,\pi^*)$ ionization suggests that there are other electron configurations involved in the cationic and/or neutral state. Within the Hartree–Fock approximation, the electronic configuration of pyrazine in its ground state (S_0) is given by

$$1b_{1u}^2 1a_g^2 1b_{2u}^2 2a_g^2 2b_{1u}^2 1b_{3g}^2 3a_g^2 3b_{1u}^2 2b_{2u}^2 4a_g^2 2b_{3g}^2 5a_g^2 3b_{2u}^2 4b_{1u}^2 4b_{2u}^2 3b_{3g}^2 \times 1b_{3u}^2(\pi) 5b_{1u}^2(n) 1b_{2g}^2(\pi) 1b_{1g}^2(\pi) 6a_g^2(n) 2b_{3u}^0(\pi^*) 1a_u^0(\pi^*) 2b_{2g}^0(\pi^*) \quad (2)$$

where nonbonding and π orbitals are respectively denoted by n and π and all other orbitals are σ orbitals. Denoting the difference from eq 2, the leading configurations of D_0 and S_2 are expressed by $6a_g^{-1}$ and $1b_{1g}^{-1}2b_{3u}^{+1}$, respectively. To enable $D_0 \leftarrow S_2$ ionization, D_0 and/or S_2 must involve minor electron configurations with a singly occupied b_{2u} orbital and two-electron excitation from the leading configuration: $jb_{2u}^{-1}1b_{1g}^{-1}2b_{3u}^{+1}$ ($j = 1$, 2, 3, and 4) and $6a_g^{-1}jb_{2u}^{+1}$ ($j \geq 5$) are the candidates for D_0 and S_2, respectively as shown in Figures 6b and 6d. In order to ascertain this speculation, we performed first-order configuration interaction and continuum multiple scattering

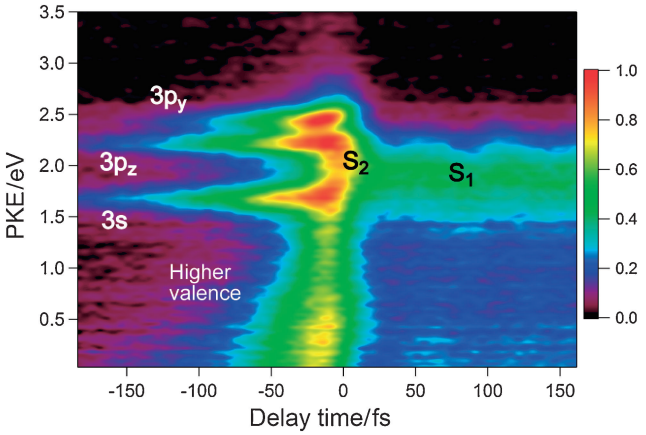

Figure 7. Photoelectron kinetic energy distribution observed using the 3ω and 5ω pulses. Positive time delays correspond to the case where the 3ω pulse precedes the 5ω pulse.

Xα (CMSXα) calculations, which indicated that the spectral intensity of $D_0 \leftarrow S_2$ is 47% from $3b_{2u}$, 27% from $4b_{2u}$, and 26% from all virtual b_{2u} (jb_{2u}, $j \geq 5$).[56]

The characteristic negative β_2 associated with the $D_0 \leftarrow S_2$ transition assisted identification of the $S_2 \rightarrow S_1$ internal conversion in pyrazine. Using CMSXα calculations, we found that β parameter diminishes with the electron kinetic energy owing to the energy-dependent Coulomb phases but β does not become negative without a shape resonance, caused by a short-lived bound electronic state buried in the ionization continuum. Our calculations indicate that there is a shape resonance at 3.5–4.0 eV above the ionization energy.[56] Aromatic molecules often have shape resonances within the range of excess energy less than 10 eV, which should be taken into account in the interpretation of TRPEI.

Figure 5b indicates that the Franck–Condon distribution upon photoionization extends toward an unobservable negative kinetic energy region. A probe photon with higher energy will enable observation of the entire Franck–Condon envelope. Thus, we revisited the same reaction using the filamentation VUV light source. TRPES of pyrazine using the 3ω pump and 5ω probe is shown in Figure 7. In the positive time delay region, photoionization from the $S_2(\pi,\pi^*)$ and $S_1(n,\pi^*)$ are clearly seen in the range of 1.5–2.5 eV. Notice that the S_1 component has shifted to higher photoelectron kinetic energies in Figure 7 in comparison with Figure 5b. Since 5ω is strongly absorbed by pyrazine, the 5ω–3ω pulse sequence also produces a signal in the negative time delay region. The three peaks in the energy range of 1.5–2.7 eV are of the 3s, 3p$_z$, and 3p$_y$ Rydberg states.[54,57] The distribution in the 0–2 eV range is due to photodissociation from higher valence states excited with 5ω, so that the photoelectron kinetic energy diminishes rapidly as the vibrational wave packet moves away from the Franck–Condon region.

2.3 $S_2 \rightarrow S_1$ Internal Conversion via Conical Intersection in Benzene and Toluene. Benzene is a benchmark aromatic molecule for theoretical and experimental studies of organic compounds. The $S_2(^1B_{1u})$ states of benzene and its derivatives are short-lived owing to ultrafast $S_2 \rightarrow S_1$ internal conversion.

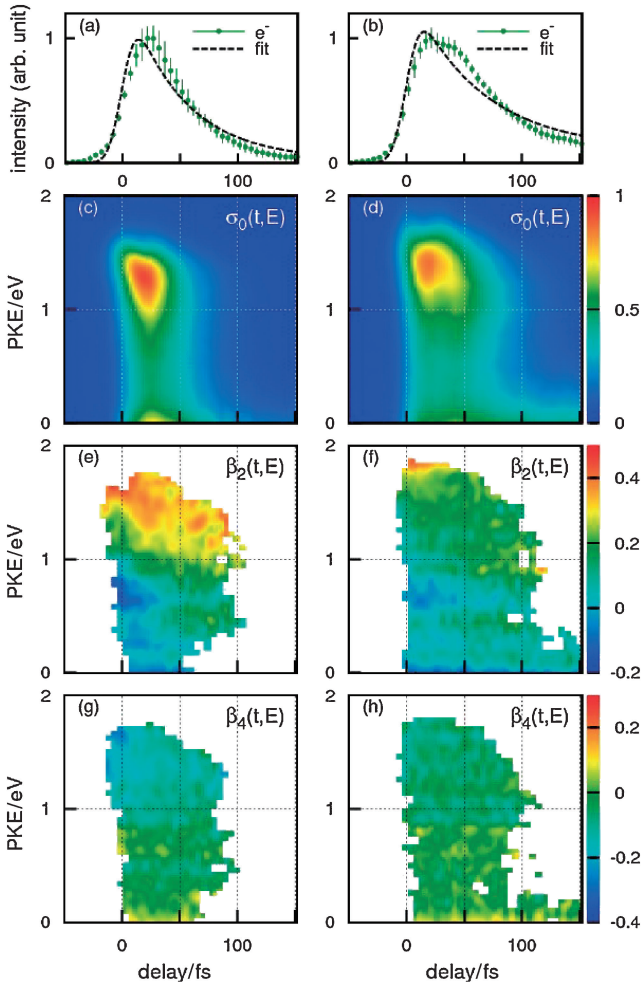

Figure 8. The time profiles of the photoionization signal intensity for (a) benzene and (b) toluene. Photoelectron signals are indicated by green dots with error bars. Time–energy maps of the photoelectron intensity, $\sigma(t,E)$, for (c) benzene and (d) toluene. Time–energy maps of the photoelectron angular anisotropies, $\beta_2(t,E)$, for (e) benzene and (f) toluene and $\beta_4(t,E)$ for (g) benzene and (h) toluene. Data points for β_2 and β_4 with standard deviations smaller than 0.2 are shown (see text). Reproduced with permission from Ref. 58.

Let us examine the dynamics in comparison with the internal conversion in pyrazine.

Figures 8a and 8b show the 4ω pump and 3ω probe TRPES of benzene and toluene, respectively.[58] The broken lines are single exponential decay functions convoluted with the cross-correlation of the pump and probe pulses. The discrepancy between the data points and the simulated curves indicate that the single exponential decay model does not adequately reproduce the observed time profiles in either case. The observed decay profiles exhibit delayed responses, which correspond to propagation of a wave packet from the Franck–Condon region to the conical intersection region. The arrival times of the wave packets at the seam of crossings are estimated as 33 fs for benzene and 41 fs for toluene: the subsequent population decay time is 32 fs for benzene and 43 fs for toluene.

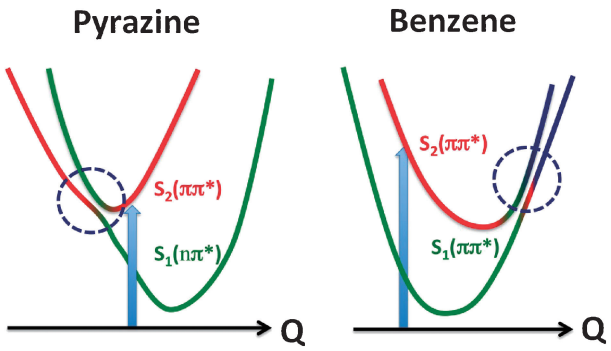

Figure 9. Comparison of conical intersections in pyrazine and benzene. The vertical arrows indicate photoexcitation, and the horizontal axes are the reaction coordinates. The red and green correspond respectively to the diabatic S_2 and S_1 states, and blue indicates contribution of other zero-order electronic states.

Figures 8c and 8d show the time evolution of photoelectron kinetic energy distributions extracted from a series of images taken at different time delays for benzene and toluene, respectively. The distributions consist of the S_2 and S_1 components that are largely different each other. The S_2 component mainly appears in the 0.5–1.5 eV range, while $S_1 < 0.3$ eV. Ionization from S_2 and S_1 occurs to the same cationic states, in which the vibrational energies are nearly conserved owing to the Franck–Condon principle upon ionization and similar potential energy surfaces between the neutrals and ions. Since internal conversion transforms the S_2–S_1 electronic energy difference into the vibrational energy in S_1, photoionization from S_1 occurs to highly vibrationally excited states of the cation leaving small photoelectron kinetic energies.[59,60] For both benzene and toluene, close examination of the high-energy (1–1.5 eV) region of the S_2 component reveals oscillatory vibrational wave packet dynamics: for example, in the case of benzene, the maximum of the energy distribution appears at 1.4 eV at 0 fs, 1.0 eV at 20 fs, and 1.3 eV at 30 fs.

Similarly to the case of pyrazine, the ultrashort S_2 lifetime implies that photoexcited benzene easily accesses an S_2/S_1 conical intersection region. Theoretical calculations predicted that the minimum-energy S_2/S_1 conical intersection point (a prefulvenic form) is close, in energy and structure, to the S_2 potential minimum.[6,61,62] The minimum, however, is at a nonplanar structure (a boat form) that differs from the planar structure of benzene (D_{6h}) in S_0.[6,61,62] Consequently, a photoexcited benzene molecule rapidly deforms from a planar structure in the Franck–Condon region toward a nonplanar structure along the steepest descent of the S_2 potential energy surface and undergoes a nonadiabatic transition in the vicinity of the S_2/S_1 seam of crossings. This is a different feature from the pyrazine case in which the Franck–Condon region is close to the minimum energy conical intersection point at the planar geometry (Figure 9). The hot S_1 benzene produced by $S_2 \rightarrow S_1$ internal conversion is further funneled down to S_0 via the S_1/S_0 conical intersection in <10 ps.[59,62,63]

Close examination of Figure 8e for benzene reveals that β_2 varies with time, most clearly around 0.7 eV; β_2 is negative at $t = 0$ and gradually increases with time to be positive around 30 fs. Similar time dependence of β_2 is also seen in Figure 8f for toluene, for example at around 1.0 eV. The evolution of $\beta_2(t,E)$ indicates that the electronic character gradually changes along the out-of-plane distortion. Notice that the out-of-plane distortion eliminates the planar symmetry and, consequently, distinction between the σ and π orbitals. Thus, different electronic states at planar geometry are mixed at nonplanar geometries: the mixing is most likely with $^1E_{1u}$ and $^1E_{2g}$.

3. Restoration of Sharp Photoelectron Angular Distribution from Broad Angular Distribution Observed for Rotating Molecules

Chemists consider reaction mechanisms having in mind the electron orbitals of a molecule fixed in space; however, real molecules are randomly oriented in gases and liquids and this leads to inevitable directional averaging in physical measurements. It is an experimental challenge to overcome this difficulty and "watch" electronic structures and dynamics in the molecular frame. In one-photon excitation of randomly oriented molecules with a linearly polarized light, photoexcited molecules are weakly aligned in space with their transition dipole moments distributed by $\cos^2\phi$ around the polarization of light, where ϕ is the angle of the transition dipole and polarization. The 4th order Legendre term in eq 1 arises from the alignment effect. However, the alignment created by one-photon excitation is so weak that, even if a photoelectron angular distribution has sharp structures in the molecular frame, the observed distribution in the laboratory frame is considerably blurred by the broad molecular axis distribution. Although even the blurred distributions provide valuable insights into nonadiabatic dynamics as discussed in the previous section, I discuss in this section restoration of a sharp photoelectron angular distribution, seen by an observer on the rotating molecule, from the blurred distributions. The key element for successful restoration is accurate information about a point-spread function, which projects a single point in the original sharp image into a finite region in a transformed (blurred) image. In the present case, the point-spread function is given by the axis alignment factor $A(t)$. The molecular axis distribution $P(\chi)$ in the laboratory frame is expressed as $P(t,\chi) = \sigma/4\pi[1 + A(t)P_2(\cos\chi)]$ using $A(t)$. The important advantage of one-photon excitation is that $A(t)$ can be rigorously calculated and reliable analysis can be performed.

In quantum mechanics, localization of a particle in a free space is realized by superposition of multiple eigenfunctions with different momenta; however, localization is nonstationary and the distribution function is rapidly broadened owing to phase dispersion of different momentum components. Likewise, sharp directional alignment or orientation of a molecule is associated with a rotational wave function with a broad angular momentum distribution. In one-photon excitation of molecules, the selection rule of $\Delta J = 0, \pm 1$ creates a superposition of only a few rotational states and a broad molecular axis distribution (J is the rotational angular momentum quantum number). The quantum mechanical interference of rotational wave functions creates peculiar time dependence of the molecular axis alignment factor, $A(t)$. Let us examine it for the $S_1(n,\pi^*) \rightarrow T_1(n,\pi^*)$ intersystem crossing in pyrazine. This process occurs in 110 ps, which is comparable to the rotational period, 82 ps, of this

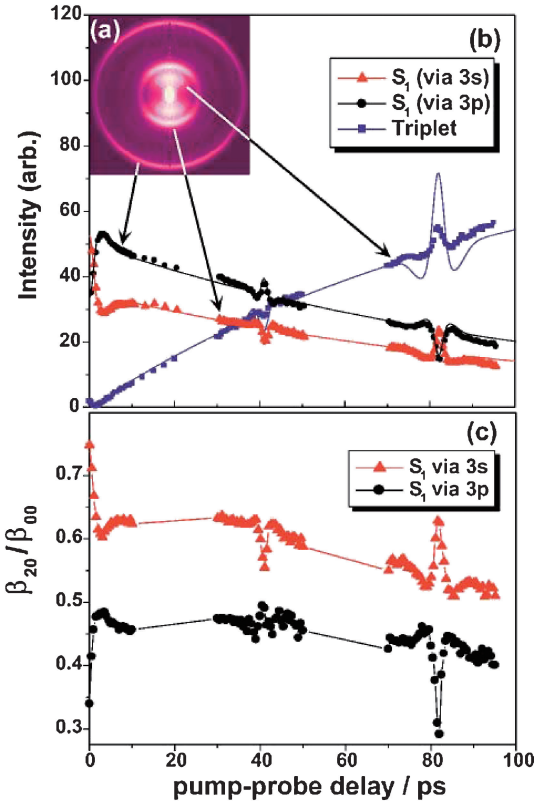

Figure 10. (a) Two-dimensional slice image of photoelectrons in the [1 + 2′] PEI of pyrazine via the S_1 $B_{3u}(n,\pi^*)$ 0° level observed at a time delay of 30 ps. The original image was integrated for 80000 laser shots. (b) Time evolution of the three major components in the [1 + 2′] PEI. Circles (●), triangles (▲), and squares (■) represent the angle-integrated intensity for the outer (PKE = 643 meV), middle (101 meV), and inner rings (37 meV), respectively. Solid lines are a simulation taking into account the rotational coherence. (c) β_{20}/β_{00} as a function of 5 defined in the text. Reproduced with permission from Ref. 64.

molecule.[28,64,65] After exciting pyrazine to the zero vibrational level in S_1, we observed two-photon ionization from the S_1 and T_1 states using the 400 nm probe pulse, in which ionization was enhanced by accidental resonance with the Rydberg states.[64] The photoelectron signal intensities of S_1 and T_1 in Figure 10b exhibit respectively a gradual decay and growth as a function of time, in which characteristic spikes due to $A(t)$ appeared (The S_1 state is probed via both 3s and 3p Rydberg states,[54,57] which exhibit opposite sign of the rotational coherence spikes). Similar signatures of $A(t)$ is also seen in the photoelectron angular anisotropies (represented by β_{20}/β_{00} in this case) in Figure 10c.

We demonstrated restoration of molecular frame photoelectron angular distribution using [1 + 1′] ionization of NO via the $A(^2\Sigma^+)$ state as an example. A free electron wave in Coulombic interactions with a diatomic cation is expressed using the electron partial waves such as sσ, pσ, pπ, and others as the standard method. We derived the formulae that relate $\sigma(t,E)$, $\beta_2(t,E)$, and $\beta_4(t,E)$ with $A(t)$ and the amplitudes and phases of partial waves,[66–68] and we measured these observables for various time-delays and probe photon energies (Figure 11). These measurements provided sufficient number of experimental observables to determine 11 values of the amplitudes and phases. We excited $NO(^2\Pi_{1/2})$ to the $A(^2\Sigma^+)$ state with a 226 nm pulse, and probed by one-photon ionization at various probe wavelengths from 323 to 242.5 nm to change the photoelectron kinetic energy from 0.05 to 1.33 eV.[67,68] One technological challenge was that the β_2, and β_4 parameters needed to be determined with accuracies of 0.01. In order to achieve this accuracy, we developed the 1 kHz CMOS camera and centroiding calculations using field programmable gate arrays and integrated each image over 10^6 laser shots.[31]

The molecular frame photoelectron angular distributions thus determined are shown in Figure 12 for two different probe photon polarization directions and photoelectron kinetic energies.[67,68] Photoionization with the polarization parallel to the bond axis induces photoemission on the oxygen side at low energy, while photoemission to the nitrogen side increases with energy. Polarization perpendicular to the bond axis creates a broad photoelectron angular distribution near the threshold, while it sharpens distributions along the probe laser polarization at higher kinetic energies.

4. Time-Resolved Photoelectron Spectroscopy of Liquids

4.1 TRPES at Ultralow Kinetic Energies. It is highly interesting to explore solution chemistry using TRPES. On the other hand, a crucial quantity in photoelectron spectroscopy of condensed matter is the escape depth of an electron. Although excitation light has a large penetration depth into the bulk material, electrons created far from the surface are unlikely to escape into vacuum owing to inelastic scattering in the bulk. The inelastic scattering cross section takes the maximum value at around 50–100 eV and diminishes in both lower and higher energy sides.[69–74] For example, Figure 13 shows the integral cross sections of the inelastic scattering of an electron, with the electron energy loss larger than 1 eV, in amorphous ice.[75] The result indicates that the cross section diminishes by nearly three orders of magnitudes for $E < 8$ eV. Thus, one may expect that the electron escape depth in liquid water increases at low electron kinetic energy. However, an electron undergoes extensive elastic scattering in liquid water at low kinetic energies, and the actual escape depth has not been determined yet. Extensive studies on the escape depth of an electron from liquid water is in progress in our laboratory; a reasonable estimate is 2–10 nm in the kinetic energy region less than 10 eV. This depth may seem rather short; however, the high relative permittivity of water effectively screens electrostatic interactions by hydration, making the liquid properties rapidly approach those of the bulk at small depths from the surface.

4.2 Charge Transfer to Solvent Reaction from I^- to Bulk Water. In order to characterize TRPES of liquids, we studied the charge transfer to solvent (CTTS) reaction from I^- to bulk water, which has previously been studied using conventional transient absorption spectroscopy.[76,77] When I^-(aq) is photoexcited to a metastable excited state below the conduction band, an excess electron cannot be ejected freely into the bulk; the electron cloud can, however, penetrate into bulk water to be trapped as a hydrated electron. Internal conversion to the ground state of I^-(aq) competes with this CTTS reaction. When accommodating the excess electron, a local hydrogen-bonding

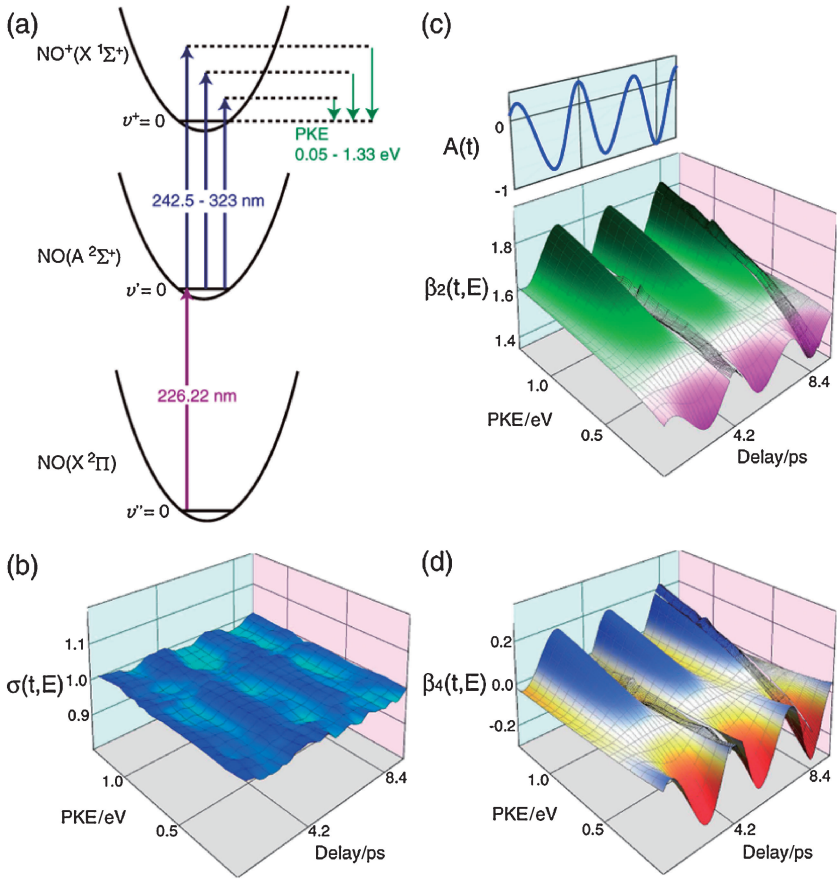

Figure 11. (a) The excitation scheme from NO ($X^2\Pi_{1/2}$, $v'' = 0$) to NO^+ ($^1\Sigma^+$, $v^+ = 0$) via the A ($^2\Sigma^+$, $v' = 0$) state. Panels (b), (c), and (d) show axis alignment factor $A(t)$ and time energy maps of photoelectron intensity and anisotropy parameters measured as functions of photoelectron kinetic energy and pump–probe time delay. $\sigma(t,E)$ in (b) represents the normalized values at each PKE. The anisotropy parameters were measured at around 4.2 and 8.4 ps with a time window of 0.6 ps, and the anisotropy parameters at other time delays were calculated from these experimental values to illustrate their time dependences. Reproduced with permission from Ref. 67.

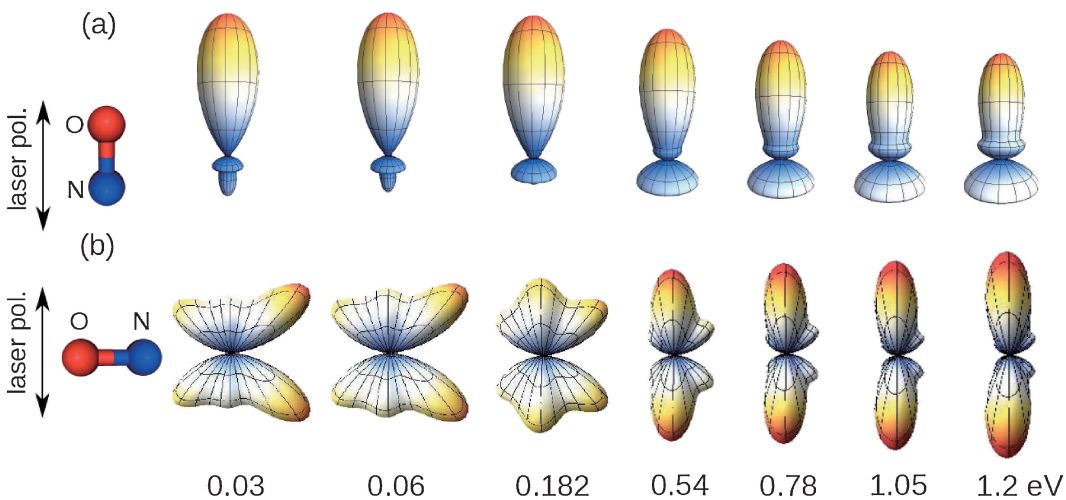

Figure 12. Molecular frame photoelectron angular distributions reconstructed from time–energy mapping of photoelectron anisotropy parameters for the σ (a) and π (b) channels. Reproduced with permission from Ref. 68.

network has to change drastically by reorienting water molecules. For the studies of CTTS dynamics strongly coupled with solvation dynamics, I^-(aq) is a suitable solute, as it has no internal degrees of freedom besides electronic motion. We excited I^-(aq) in water with a pump pulse (243–226 nm) and photodetached negatively charged transients with a time-delayed 260 nm probe pulse (Figure 14).[19] Figure 15 shows the photoelectron spectrum measured as a function of the time

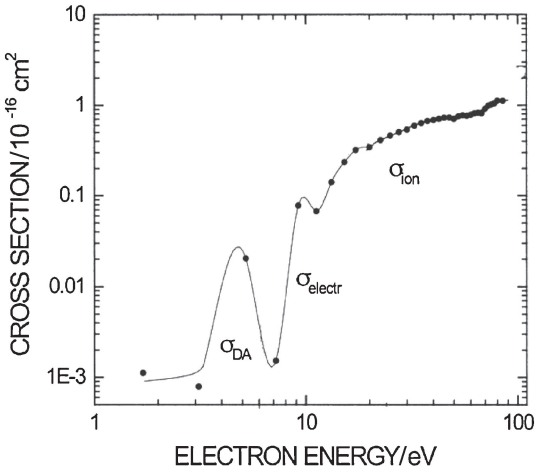

Figure 13. Integral cross section (shown by dots) ascribed to the sum of dissociative attachment (DA), vibrational excitation above 1 eV energy loss, electronic excitations (electr), as well as ionization (ion) processes in amorphous ice. Adopted from Ref. 75.

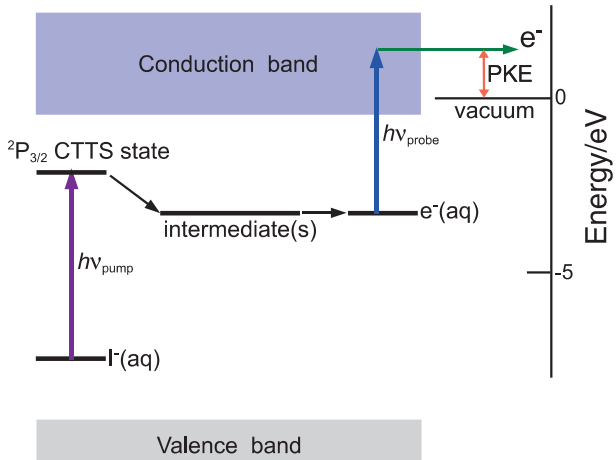

Figure 14. Schematic energy diagram for time-resolved photoelectron spectroscopy of a charge transfer to solvent (CTTS) reaction. Reproduced with permission from Ref. 78.

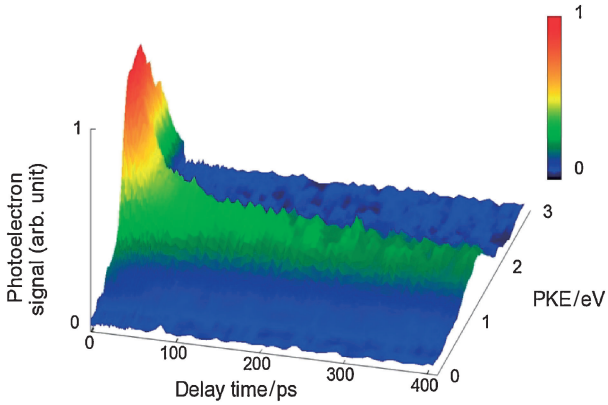

Figure 15. 3D plot of the photoelectron kinetic energy distribution as a function of time in [1 + 1′] TRPES of 0.14 M aqueous NaI solution. The pump and probe wavelengths are 243 and 260 nm, respectively. Reproduced with permission from Ref. 19.

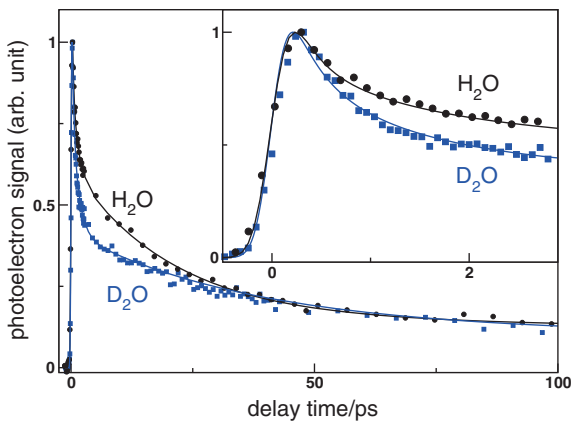

Figure 16. Photoelectron signal intensity as a function of pump–probe time delay observed for the charge transfer to solvent (CTTS) reaction of I^- to bulk water: the sample solutions were 0.1 M aqueous NaI solution in H_2O (black) and D_2O (blue). The schematic energy diagram of the experiment is shown in Figure 14. The cross correlation of the pump and probe laser pulses was ca. 300 fs. A hemispherical electron energy analyzer was used to measure a photoelectron spectrum at each time delay, and the spectrum was integrated over photoelectron kinetic energy to obtain the each data point. Reproduced with permission from Ref. 78.

delay. The energy spectrum is initially broad, but the width diminishes rapidly and the intensity decreases gradually. If electron inelastic scattering in water is extensive, the photoelectron kinetic energy distribution should exhibit a decelerated component irrespective of the pump–probe time delay. However, the result exhibits no signature of decelerated electrons, indicating that the influence of inelastic scattering on the energy distribution can be neglected.

Figure 16 shows the total electron intensity observed as a function of delay time for the CTTS reactions in H_2O and D_2O.[78] The decay profiles clearly indicate that there are at least three elementary steps involved in the CTTS reaction, and the time constants are different between the two solvents. The time-dependences of the photoelectron signal intensity and spectral shifts are explained by a model assuming two reaction intermediates of a solvent separated and contact pair states.[78] The observed decay is ascribed to geminate recombination of an electron with a neutral iodine atom from the CTTS, solvent separated, and contact pair state. The time constants extracted from TRPES (Figure 17) are in good agreement with those from transient absorption spectroscopy.[76,77] Thus, although the probing depth of TRPES is not established yet, it is strongly suggested that TRPES at ultralow kinetic energy (<5 eV) probes bulk solution chemistry.

4.3 Electron-Binding Energies of Solvated Electrons. The CTTS reaction in bulk water discussed in the preceding section ultimately creates hydrated electrons.[19,79–98] The hydrated electron is the most important transient species in radiation chemistry and biology; its electron-binding energy, however, has not been measured by any methods. In the 1990s,

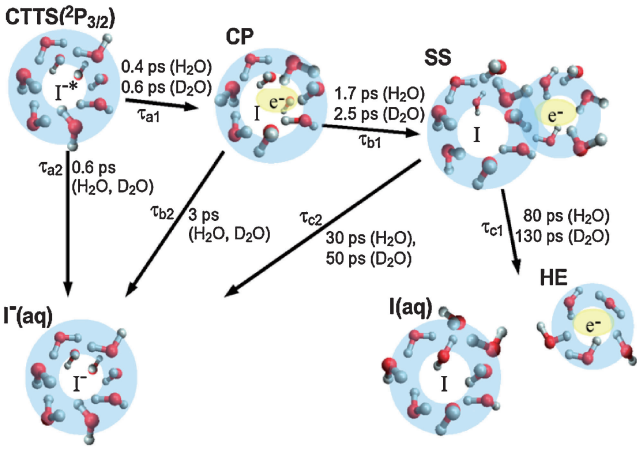

Figure 17. Graphical presentation of our kinetic model with some representative time constants for the charge transfer to solvent (CTTS) reaction of I^- to bulk water. The observed experimental results can be explained equally well by a kinetic model presented here and a diffusion model. The latter involves solving a diffusion equation with an assumed interaction potential, e.g., a Morse potential. Reproduced with permission from Ref. 78.

researchers found that the electron-binding energy of negatively charged water clusters varies approximately as $n^{1/3}$ where n is the number of water molecules in the cluster. This trend agrees qualitatively with a model of an electron in a spherical dielectric cavity. In the 1990s, the electron-binding energy of a hydrated electron in bulk water was estimated to be 3.3 eV by extrapolating the vertical electron-binding energies of negatively charged water clusters to the infinitely large size of the cluster.[87] Theoretical calculations, however, have refuted this estimate by showing that the electron-binding energy varies with $n^{1/3}$ even when the excess electron is trapped at the surfaces of clusters.[90,99,100] Since the cluster anions are generated by electron attachment to cold neutral clusters in molecular beams, the energetic penalty is large for an excess electron to penetrate into a cluster by disrupting the hydrogen-bonding network; consequently, an electron is trapped at the surface of cold clusters. Later studies have shown that there are three different isomers (I–III) for negatively charged water clusters. The isomers I–III have three different asymptotic values of electron-binding energies at the infinitely large sizes of the clusters, in which isomer I is regarded as a precursor of a hydrated electron in the bulk,[101] while isomer II seems related to a hypothesized surface state of a hydrated electron.[102,103] A more recent study has revealed that the isomer I has two different species known as isomer Ia and Ib; the extrapolation of the electron-binding energy to the infinite cluster size of Ib is in the region of 3.5–4.0 eV (Figure 18).[94,104]

Our first TRPES experiment of aqueous NaI solution estimated the vertical electron-binding energy of a hydrated electron in bulk water to be 3.3 eV (Figure 15),[19] in excellent agreement with the estimate made from the cluster values.[86,87] However, a low signal-to-noise ratio and electrokinetic charging of a liquid beam limited the accuracy. In order to achieve higher precision and reliability for liquid TRPES, we have constructed a magnetic bottle time-of-flight (TOF) spectrometer

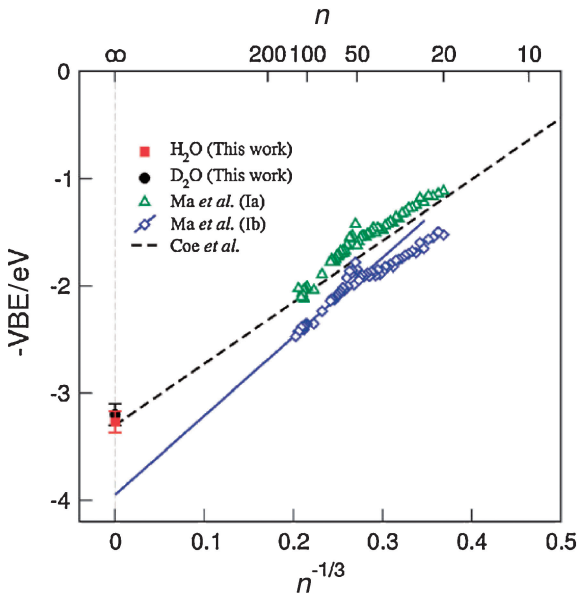

Figure 18. Vertical binding energy of a hydrated electron in bulk water observed in this work compared with the cluster values by Ma et al.[104] The original extrapolation by Coe et al. is also indicated by a broken line.[87] Reproduced with permission from Ref. 19.

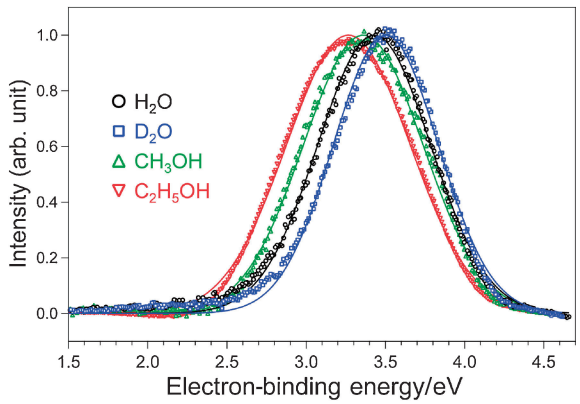

Figure 19. Photoelectron spectra of solvated electrons in bulk solutions: H_2O (black), D_2O (blue), methanol (green), and ethanol (red). Open circles are experimental data and solid lines are the best-fit Gaussian functions obtained by least-squares fitting. There was no signal in the energy region of 0–1.5 eV. Reproduced with permission from Ref. 105.

(flight length: 1 m), which collects 50% of photoelectrons emitted from the liquid beam and enables measurement of the entire photoelectron energy spectrum on a shot-to-shot basis.[105] In combination with a 100 kHz DUV femtosecond laser we constructed, the new spectrometer improved the signal count level by four to five orders of magnitude in comparison with our old system. The spectra of solvated electrons in H_2O, D_2O, methanol, and ethanol measured at a pump–probe time delay of 2 ns are shown in Figure 19. A striking feature of these spectra is their symmetric Gaussian shapes: the photoabsorption spectra of solvated electrons in bulk solutions as well as photoelectron spectra of water cluster anions exhibit asym-

Table 1. Vertical Binding Energies (eV) of Solvated Electrons

Solvent	Liquid	Estimate from cluster anion
H_2O	3.4	3.3 (Ia)[a], 4.0 (Ib)[b]
D_2O	3.5	—
Methanol	3.4	2.6[c]
Ethanol	3.3	—

a) Ref. 87. b) Ref. 104. c) Ref. 106.

metric band shapes, which are fit by a Gaussian and Lorentzian. The electron-binding energies of solvated electrons determined from these high-precision measurements are listed in Table 1.

As seen in Table 1, the electron-binding energy of a solvated electron in methanol is 3.4 eV, which is clearly larger than the value, 2.6 eV, estimated from the methanol cluster data.[106] The result indicates that the excellent agreement between the electron-binding energy of a hydrated electron in bulk solution and the estimate from water cluster anions cannot be generalized to other solvents. Molecular cluster anions produced in supersonic molecular beams are at ultralow temperatures, and their thermodynamic properties are generally different from bulk solution at an ambient temperature. Therefore, it is possible that the agreement observed for water is fortuitous.

5. Summary

Time-resolved photoelectron imaging (TRPEI) enables efficient and accurate measurements of photoelectron energy and angular distributions as a function of the pump–probe time delay. Time–energy mapping of photoelectron angular anisotropy clearly reveals rapid changes of electron configuration during the course of photoinduced dynamics. The S_2 state of pyrazine exhibited immediate population decay from the Franck–Condon region, while the S_2 state of benzene and toluene decayed after finite induction time due to wave packet motions from the Franck–Condon region to conical intersection region. The results illustrate the importance of the locations of the conical intersections on the potential energy surfaces in internal conversion dynamics. It has been shown that the photoelectron angular anisotropy is influenced by shape resonances with metastable bound states in the continuum.

Time-resolved photoelectron spectroscopy (TRPES) of liquids provides new opportunities for ultrafast spectroscopic studies of electron dynamics under wet conditions. TRPES of the charge transfer to solvent reaction from I^- to bulk water well demonstrated the usefulness of this methodology for the studies of solution chemistry. The electron-binding energies of solvated electrons in four polar protic solvents were firmly established by liquid TRPES. The method is expected to be particularly useful for elucidating electron-transfer processes and redox reactions. Similarly with TRPES in the gas phase, the time–energy mapping of photoelectron angular anisotropy becomes an invaluable tool in studying electronic dynamics in solution, and its technical development is underway in our laboratory.

I would like to thank my present and past group members who made great contribution to TRPES in our laboratory, Y. Suzuki, T. Fuji, Y. Tang, T. Horio, H. Kohguchi, Y. Ogi, S.-Y. Liu, H. Shen, K. Sekiguchi, and N. Kurahashi. I also thank Professors V. Bonacic-Koutechy and R. Mitiric for collaboration on molecular dynamics on the fly.

References

1 M. Born, R. Oppenheimer, *Ann. Phys.* **1927**, *389*, 457.
2 E. Teller, *Isr. J. Chem.* **1969**, *7*, 227.
3 L. Salem, *J. Am. Chem. Soc.* **1974**, *96*, 3486.
4 L. Salem, C. Leforestier, G. Segal, R. Wetmore, *J. Am. Chem. Soc.* **1975**, *97*, 479.
5 J. Michl, V. Bonacic-Koutecky, *Electronic Aspects of Organic Photochemistry*, Wiley-Interscience Publication, **1990**.
6 I. J. Palmer, I. N. Ragazos, F. Bernardi, M. Olivucci, M. A. Robb, *J. Am. Chem. Soc.* **1993**, *115*, 673.
7 C. Nordling, E. Sokolowski, K. Siegbahn, *Phys. Rev.* **1957**, *105*, 1676.
8 D. W. Turner, M. I. Al Jobory, *J. Chem. Phys.* **1962**, *37*, 3007.
9 F. I. Vilesov, A. N. Terenin, B. L. Kurbatoy, *Dokl. Akad. Nauk SSSR* **1961**, *138*, 1329.
10 K. Siegbahn, *J. Electron Spectrosc. Relat. Phenom.* **1985**, *36*, 113.
11 J. L. Knee, in *High Resolution Laser Photoionization and Photoelectron Studies*, ed. by I. Powis, T. Baer, C.-Y. Ng, John Wiley & Sons, **1995**.
12 I. V. Hertel, W. Radloff, *Rep. Prog. Phys.* **2006**, *69*, 1897.
13 T. Seideman, *Annu. Rev. Phys. Chem.* **2002**, *53*, 41.
14 K. L. Reid, *Int. Rev. Phys. Chem.* **2008**, *27*, 607.
15 A. Stolow, A. E. Bragg, D. M. Neumark, *Chem. Rev.* **2004**, *104*, 1719.
16 H. Siegbahn, *J. Phys. Chem.* **1985**, *89*, 897.
17 M. Faubel, S. Schlemmer, J. P. Toennies, *Z. Phys. D: At., Mol. Clusters* **1988**, *10*, 269.
18 K. R. Wilson, B. S. Rude, J. Smith, C. Cappa, D. T. Co, R. D. Schaller, M. Larsson, T. Catalano, R. J. Saykally, *Rev. Sci. Instrum.* **2004**, *75*, 725.
19 Y. Tang, H. Shen, K. Sekiguchi, N. Kurahashi, T. Mizuno, Y.-I. Suzuki, T. Suzuki, *Phys. Chem. Chem. Phys.* **2010**, *12*, 3653.
20 Y. Tang, Y.-i. Suzuki, H. Shen, K. Sekiguchi, N. Kurahashi, K. Nishizawa, P. Zuo, T. Suzuki, *Chem. Phys. Lett.* **2010**, *494*, 111.
21 P. Kruit, F. H. Read, *J. Phys. E: Sci. Instrum.* **1983**, *16*, 313.
22 D. W. Chandler, P. L. Houston, *J. Chem. Phys.* **1987**, *87*, 1445.
23 A. T. J. B. Eppink, D. H. Parker, *Rev. Sci. Instrum.* **1997**, *68*, 3477.
24 J. J. Lin, J. Zhou, W. Shiu, K. Liu, *Rev. Sci. Instrum.* **2003**, *74*, 2495.
25 S.-Y. Liu, K. Alnama, J. Matsumoto, K. Nishizawa, H. Kohguchi, Y.-P. Lee, T. Suzuki, *J. Phys. Chem. A* **2011**, *115*, 2953.
26 T. Suzuki, L. Wang, H. Kohguchi, *J. Chem. Phys.* **1999**, *111*, 4859.
27 L. Wang, H. Kohguchi, T. Suzuki, *Faraday Discuss.* **1999**, *113*, 37.
28 T. Suzuki, in *Modern Trends in Chemical Reaction Dynamics: Experiment and Theory (Part I)*, ed. by C.-Y. Ng, World Scientific, Singapore, **2004**.
29 T. Suzuki, *Annu. Rev. Phys. Chem.* **2006**, *57*, 555.
30 T. Suzuki, *Int. Rev. Phys. Chem.* **2012**, *31*, 265.
31 T. Horio, T. Suzuki, *Rev. Sci. Instrum.* **2009**, *80*, 013706.
32 T. Fuji, T. Horio, T. Suzuki, *Opt. Lett.* **2007**, *32*, 2481.
33 T. Fuji, T. Suzuki, E. E. Serebryannikov, A. Zheltikov,

Phys. Rev. A **2009**, *80*, 063822.
34 P. Zuo, T. Fuji, T. Horio, S. Adachi, T. Suzuki, *Appl. Phys. B* **2012**, *108*, 815.
35 S. L. Chin, *Femtosecond Laser Filamentation* in *Springer Series on Atomic, Optical, and Plasma Physics*, Springer, New York, **2010**. doi:10.1007/978-1-4419-0688-5.
36 R. Schneider, W. Domcke, *Chem. Phys. Lett.* **1988**, *150*, 235.
37 L. Seidner, G. Stock, A. L. Sobolewski, W. Domcke, *J. Chem. Phys.* **1992**, *96*, 5298.
38 C. Woywod, W. Domcke, A. L. Sobolewski, H.-J. Werner, *J. Chem. Phys.* **1994**, *100*, 1400.
39 T. Gerdts, U. Manthe, *Chem. Phys. Lett.* **1998**, *295*, 167.
40 A. Raab, G. A. Worth, H.-D. Meyer, L. S. Cederbaum, *J. Chem. Phys.* **1999**, *110*, 936.
41 M. Thoss, W. H. Miller, G. Stock, *J. Chem. Phys.* **2000**, *112*, 10282.
42 C. Coletti, G. D. Billing, *Chem. Phys. Lett.* **2003**, *368*, 289.
43 D. V. Shalashilin, M. S. Child, *J. Chem. Phys.* **2004**, *121*, 3563.
44 X. Chen, V. S. Batista, *J. Chem. Phys.* **2006**, *125*, 124313.
45 P. Puzari, B. Sarkar, S. Adhikari, *J. Chem. Phys.* **2006**, *125*, 194316.
46 P. Puzari, R. S. Swathi, B. Sarkar, S. Adhikari, *J. Chem. Phys.* **2005**, *123*, 134317.
47 R. He, C. Zhu, C.-H. Chin, S. H. Lin, *Chem. Phys. Lett.* **2009**, *476*, 19.
48 U. Werner, R. Mitrić, T. Suzuki, V. Bonačić-Koutecký, *Chem. Phys.* **2008**, *349*, 319.
49 U. Werner, R. Mitrić, V. Bonačić-Koutecký, *J. Chem. Phys.* **2010**, *132*, 174301.
50 C.-K. Lin, Y. Niu, C. Zhu, Z. Shuai, S. H. Lin, *Chem.—Asian J.* **2011**, *6*, 2977.
51 M. Seel, W. Domcke, *J. Chem. Phys.* **1991**, *95*, 7806.
52 Y.-I. Suzuki, T. Fuji, T. Horio, T. Suzuki, *J. Chem. Phys.* **2010**, *132*, 174302.
53 V. Stert, P. Farmanara, W. Radloff, *J. Chem. Phys.* **2000**, *112*, 4460.
54 M. Oku, Y. Hou, X. Xing, B. Reed, H. Xu, C. Chang, C.-Y. Ng, K. Nishizawa, K. Ohshimo, T. Suzuki, *J. Phys. Chem. A* **2008**, *112*, 2293.
55 K. K. Innes, I. G. Ross, W. R. Moomaw, *J. Mol. Spectrosc.* **1988**, *132*, 492.
56 Y.-I. Suzuki, T. Suzuki, *J. Chem. Phys.* **2012**, *137*, 194314.
57 J. K. Song, M. Tsubouchi, T. Suzuki, *J. Chem. Phys.* **2001**, *115*, 8810.
58 Y.-I. Suzuki, T. Horio, T. Fuji, T. Suzuki, *J. Chem. Phys.* **2011**, *134*, 184313.
59 W. Radloff, V. Stert, Th. Freudenberg, I. V. Hertel, C. Jouvet, C. Dedonder-Lardeux, D. Solgadi, *Chem. Phys. Lett.* **1997**, *281*, 20.
60 P. Farmanara, V. Stert, W. Radloff, I. V. Hertel, *J. Phys. Chem. A* **2001**, *105*, 5613.
61 M. Meisl, R. Janoschek, *J. Chem. Soc., Chem. Commun.* **1986**, 1066.
62 A. Toniolo, A. L. Thompson, T. J. Martínez, *Chem. Phys.* **2004**, *304*, 133.
63 W. Radloff, T. Freudenberg, H.-H. Ritze, V. Stert, F. Noack, I. V. Hertel, *Chem. Phys. Lett.* **1996**, *261*, 301.
64 M. Tsubouchi, B. J. Whitaker, L. Wang, H. Kohguchi, T. Suzuki, *Phys. Rev. Lett.* **2001**, *86*, 4500.
65 T. Suzuki, L. Wang, M. Tsubouchi, *J. Phys. Chem. A* **2004**, *108*, 5764.
66 Y.-I. Suzuki, T. Suzuki, *Mol. Phys.* **2007**, *105*, 1675.
67 Y. Tang, Y.-I. Suzuki, T. Horio, T. Suzuki, *Phys. Rev. Lett.* **2010**, *104*, 073002.
68 Y.-I. Suzuki, Y. Tang, T. Suzuki, *Phys. Chem. Chem. Phys.* **2012**, *14*, 7309.
69 M. P. Seah, W. A. Dench, *Surf. Interface Anal.* **1979**, *1*, 2.
70 T. L. Barr, *Modern ESCA: The Principles and Practice of X-Ray Photoelectron Spectroscopy*, CRC Press Inc., **1994**.
71 S. Hüfner, *Photoelectron Spectroscopy: Principles and Applications* in *Advanced Texts in Physics*, Springer-Verlag, **2003**. doi:10.1007/978-3-662-09280-4.
72 D. Emfietzoglou, I. Kyriakou, I. Abril, R. Garcia-Molina, H. Nikjoo, *Int. J. Radiat. Biol.* **2012**, *88*, 22.
73 D. Emfietzoglou, I. Kyriakou, I. Abril, R. Garcia-Molina, I. D. Petsalakis, H. Nikjoo, A. Pathak, *Nucl. Instrum. Methods Phys. Res., Sect. B* **2009**, *267*, 45.
74 N. Ottosson, M. Faubel, S. E. Bradforth, P. Jungwirth, B. Winter, *J. Electron Spectrosc. Relat. Phenom.* **2010**, *177*, 60.
75 M. Michaud, A. Wen, L. Sanche, *Radiat. Res.* **2003**, *159*, 3.
76 J. A. Kloepfer, V. H. Vilchiz, V. A. Lenchenkov, X. Chen, S. E. Bradforth, *J. Chem. Phys.* **2002**, *117*, 766.
77 H. Iglev, A. Trifonov, A. Thaller, I. Buchvarov, T. Fiebig, A. Laubereau, *Chem. Phys. Lett.* **2005**, *403*, 198.
78 Y.-I. Suzuki, H. Shen, Y. Tang, N. Kurahashi, K. Sekiguchi, T. Mizuno, T. Suzuki, *Chem. Sci.* **2011**, *2*, 1094.
79 E. J. Hart, J. W. Boag, *J. Am. Chem. Soc.* **1962**, *84*, 4090.
80 M. Natori, T. Watanabe, *J. Phys. Soc. Jpn.* **1966**, *21*, 1573.
81 S. Schlick, P. A. Narayana, L. Kevan, *J. Chem. Phys.* **1976**, *64*, 3153.
82 F. J. Webster, J. Schnitker, M. S. Friedrichs, R. A. Friesner, P. J. Rossky, *Phys. Rev. Lett.* **1991**, *66*, 3172.
83 J. Schnitker, K. Motakabbir, P. J. Rossky, R. A. Friesner, *Phys. Rev. Lett.* **1988**, *60*, 456.
84 P. J. Rossky, J. Schnitker, *J. Phys. Chem.* **1988**, *92*, 4277.
85 J. Schnitker, P. J. Rossky, *J. Chem. Phys.* **1987**, *86*, 3471.
86 A. E. Bragg, J. R. R. Verlet, A. Kammrath, O. Cheshnovsky, D. M. Neumark, *Science* **2004**, *306*, 669.
87 J. V. Coe, G. H. Lee, J. G. Eaton, S. T. Arnold, H. W. Sarkas, K. H. Bowen, C. Ludewigt, H. Haberland, D. R. Worsnop, *J. Chem. Phys.* **1990**, *92*, 3980.
88 M. J. Tauber, R. A. Mathies, *J. Phys. Chem. A* **2001**, *105*, 10952.
89 M. Mizuno, T. Tahara, *J. Phys. Chem. A* **2001**, *105*, 8823.
90 L. Turi, W.-S. Sheu, P. J. Rossky, *Science* **2005**, *309*, 914.
91 I. A. Shkrob, *J. Phys. Chem. A* **2007**, *111*, 5223.
92 I. A. Shkrob, W. J. Glover, R. E. Larsen, B. J. Schwartz, *J. Phys. Chem. A* **2007**, *111*, 5232.
93 R. E. Larsen, W. J. Glover, B. J. Schwartz, *Science* **2010**, *329*, 65.
94 L. D. Jacobson, J. M. Herbert, *J. Am. Chem. Soc.* **2011**, *133*, 19889.
95 J. M. Herbert, L. D. Jacobson, *Int. Rev. Phys. Chem.* **2011**, *30*, 1.
96 K. R. Siefermann, Y. Liu, E. Lugovoy, O. Link, M. Faubel, U. Buck, B. Winter, B. Abel, *Nat. Chem.* **2010**, *2*, 274.
97 A. T. Shreve, T. A. Yen, D. M. Neumark, *Chem. Phys. Lett.* **2010**, *493*, 216.
98 A. Lübcke, F. Buchner, N. Heine, I. V. Hertel, T. Schultz, *Phys. Chem. Chem. Phys.* **2010**, *12*, 14629.
99 O. Marsalek, F. Uhlig, T. Frigato, B. Schmidt, P. Jungwirth, *Phys. Rev. Lett.* **2010**, *105*, 043002.

100 O. Marsalek, F. Uhlig, P. Jungwirth, *J. Phys. Chem. C* **2010**, *114*, 20489.
101 J. V. Coe, S. M. Williams, K. H. Bowen, *Int. Rev. Phys. Chem.* **2008**, *27*, 27.
102 J. R. R. Verlet, A. E. Bragg, A. Kammrath, O. Cheshnovsky, D. M. Neumark, *Science* **2005**, *307*, 93.
103 J. R. R. Verlet, A. E. Bragg, A. Kammrath, O. Cheshnovsky, D. M. Neumark, *Science* **2005**, *310*, 1769.
104 L. Ma, K. Majer, F. Chirot, B. von Issendorff, *J. Chem. Phys.* **2009**, *131*, 144303.
105 T. Horio, H. Shen, S. Adachi, T. Suzuki, *Chem. Phys. Lett.* **2012**, *535*, 12.
106 A. Kammrath, J. R. R. Verlet, G. B. Griffin, D. M. Neumark, *J. Chem. Phys.* **2006**, *125*, 171102.

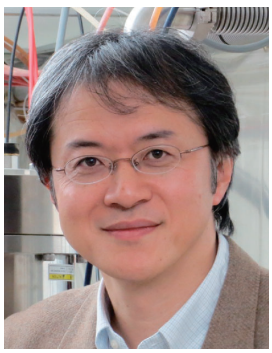

Toshinori Suzuki obtained his Ph.D. degree in 1988 from Tohoku University. He then became a research associate at the Institute for Molecular Science (IMS), between 1988 and 1990, and a JSPS fellow for research abroad to carry out research on molecular beam scattering at Cornell University and the University of California, Berkeley, between 1990 and 1992. He returned to Japan as an associate professor at IMS, where he started his independent research group on chemical reaction dynamics in 1992. In 2001, he moved to RIKEN to be a chief scientist and extended his research further. In 2009, he became a professor of physical chemistry at Kyoto University to educate the next leaders of Japanese science, and from 2012, he is serving as a Chair of the Division of Chemistry, Graduate School of Science. He received Broida Award, IBM Science Award, JSPS Award, Commendation for Science and Technology by MEXT.